Prediction of EVE/ESP Irradiance from SDO/AIA Images using Fuzzy Image Processing and Machine Learning

T. Colak and R. Qahwaji

Centre for Visual Computing

University of Bradford, Richmond Road, Bradford BD7 1DP, England, UK

(E-mail: t.colak@bradford.ac.uk, r.s.r.qahwaji@bradford.ac.uk)

Abstract. The cadence and resolution of solar images have been increasing dramatically with the launch of new satellites such as STEREO and SDO. This increase in data volumes provides new opportunities for solar researchers, but the efficient processing and analysis of these data create new challenges. In this paper a fuzzy-based solar feature detection system is introduced. The proposed system processes SDO/AIA images using fuzzy rules to detect coronal holes and active regions. This system is fast and it can handle different size images. It is tested on six months (1st October 2010 to 31st March 2011) of solar data to generate filling factors (ratio of area of solar feature to area of rest of the solar disk) for active regions and coronal holes. These filling factors are then compared to SDO/EVE/ESP irradiance measurements data. Correlation between active region filling factors and irradiance measurements data is found to be very high which has encouraged us to design a time series prediction system using Radial Basis Function Networks to predict ESP irradiance measurements from our generated filling factors.

1. Introduction

The cadence and quality of solar images have been increasing dramatically, especially with the launch of *Solar TErrestrial RElations Observatory* (STEREO) and *Solar Dynamics Observatory* (SDO) satellites. Although this increase in data, opens new opportunities for investigating different solar phenomena and unveiling the secrets of the Sun, compared to older satellites such as *Solar and Heliospheric Observatory* (SOHO) and ground based observatories, it is becoming impossible to manually investigate and analyse all the available solar images.

The majority of existing solar imaging systems focus on detecting individual solar features and processing specific wave-length images. A comprehensive overview of solar image processing techniques that are used in automated solar feature-detection algorithms is presented in {Aschwanden, 2009 #284}. Most of the algorithms developed so far are complex and most importantly depends on empirically determined values. Also many existing algorithms are optimized for specific image sizes, wave-lengths and/or certain solar features.

In this paper a system that uses fuzzy image processing and machine learning to predict solar irradiance is introduced. Once trained properly, fuzzy image processing can be used to detect almost any desired solar feature from almost any type of solar images in a relatively short time. Fuzzy systems can process different-size images and its feature detection time changes linearly with respect to the size of the image.

This is not the first time fuzzy theory is applied to solar images. {Revathy, 2005 #282}applied a fractal-based fuzzy technique to several channel (30.4, 17.1, and 28.4 nm) of SOHO *Extreme ultraviolet Imaging Telescope* (EIT) images to identify active regions and study their characteristics. They concluded that the advantage of such a fuzzy-based segmentation lies in the fact that the grade of membership functions labels the pixels into either active or non-active region without further computation, as needed for other segmentation algorithms like neural network, clustering. {Barra, 2008 #281} and {Barra, 2009 #278} applied unsupervised fuzzy clustering to two channels of SOHO/EIT images at the same time. They detected quite sun, coronal holes and active regions using unsupervised Fuzzy C- Means algorithm and analyzed all the EIT 17.1 and 19.5 nm images for solar cycle 23.
In {Barra, 2008 #281} two channels from SOHO/EIT images, with a maximum time difference of 30 minutes, were processed simultaneously. In this study a supervised fuzzy algorithm is developed to simultaneously process three channels of SDO *Atmospheric Imaging Assembly* (AIA) images, separated by a maximum time difference of one minute. This allowed us to investigate the relationship between coronal holes and active regions with irradiance at micro level.
Once the method has been trained and the fuzzy classes are defined the method is fast and can handle images of different sizes. It is tested on six months period (1stOctober 2010 to 31st March 2011) of solar images and filling factors (ratio of area of solar feature to area of entire solar disk) for active regions and coronal holes are calculated. These filling factors are then compared to two channels (ESP 171 and ESP 257) of SDO *Extreme Ultraviolet Variablity Experiment* (EVE) irradiance data for the same time period.
Also a Radial Basis Function Network (RBFN) is trained with filling factors extracted from the AIA images and used for time series prediction of irradiance. The aim of a time series prediction system is to predict future events based on known past events. RBFN have proven to work well for short-term time series forecasting techniques {Awad, 2009 #296} and therefore we decided to implement this model for irradiance prediction.
This paper is organized as follows: Section 2 provides brief description for the SDO data used in this work. In section 3, fuzzy solar imaging system is introduced. Section 4 provides a comparison between the extracted data from solar images and their corresponding solar irradiance measurements from EVE. The time-series prediction using RBFN is introduced in Section 5 followed by the conclusions.

2. Data

In this work, several channels (wavelengths) of solar images from the SDO/AIA instrument are used for active region and coronal-hole segmentation. The SDO satellite was launched on 2010. SDO produces 1-2 TBytes of data per day, which includes 4k × 4k images of the full Sun in ten EUV and UV wavelengths covering a wide range of temperatures every ten seconds. This exceeds by a factor 1000 the volume from its predecessor SOHO. Three AIA channels; 193, 304, and 1700 are selected and processed simultaneously in this work. These channels are selected because the coronal holes, active regions and solar disk are visually distinguishable in AIA 193, 304 and 1700, respectively. Figure 1 shows these images. For this work AIA images in JPEG format which are downloaded from http://sdo.gsfc.nasa.gov/assets/img/browse/are used. It is also worth mentioning

that if FITS images were used, the solar disk could be determined by the keywords of the FITS header and in practice the AIA 1700 channel could be omitted from this study.
Also solar irradiance data from the EVE instrument on board SDO is used for investigating the relations between the detected solar features and EUV irradiance. EVE, which is designed to measure the EUV irradiance, contains the *Extreme Ultraviolet Spectrophotometer* (ESP) {Didkovsky, 2009 #290}, an instrument to record the intensity of solar ultraviolet radiation over time in five wavelength bands in the extreme ultraviolet (EUV) spectral region. The EUV radiation includes the 0.1-105 nm range, which provides the majority of the energy for heating Earth's thermosphere and creating Earth's ionosphere (ionized plasma). EVE's wide spectral range requires the use of multiple channels and this data is freely available in (http://lasp.colorado.edu/eve/data/quicklook/L0CS/). In this study two channels (ESP 171 and 257) of EVE are used.

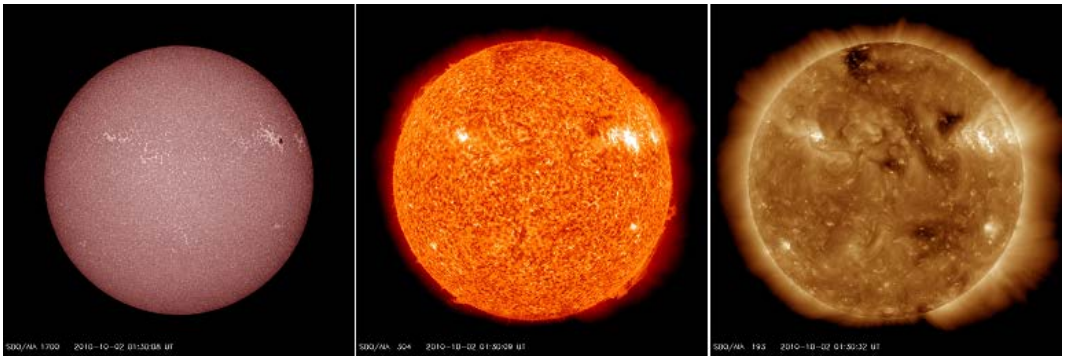

Figure 1: From left to right SDO AIA 1700, 304, and 193 images.

2.1 Challenges in Data Preparation

For detecting active regions and coronal holes, three channels (193, 304, and 1700) of 1K × 1K AIA images with 10 to 15 minutes cadence is used. Downloading and processing these images were very challenging due to the huge amount of data involved. There are around 45000 (3 channels) images for the six-month period and a python based script is written to automatically download these images. It takes nearly one day to download these images. Once the download was complete all these images needed to be checked for data corruption. Checking these images manually could be very time consuming and a computer program was needed to automatically investigate these images and ensure they were suitable for our study.
A simple program which can check these images for certain types of corruption and irregularities such as images with no solar disk and non-round solar disk images is created. Figure 2 shows some corrupted images that can be found on the downloaded AIA images.

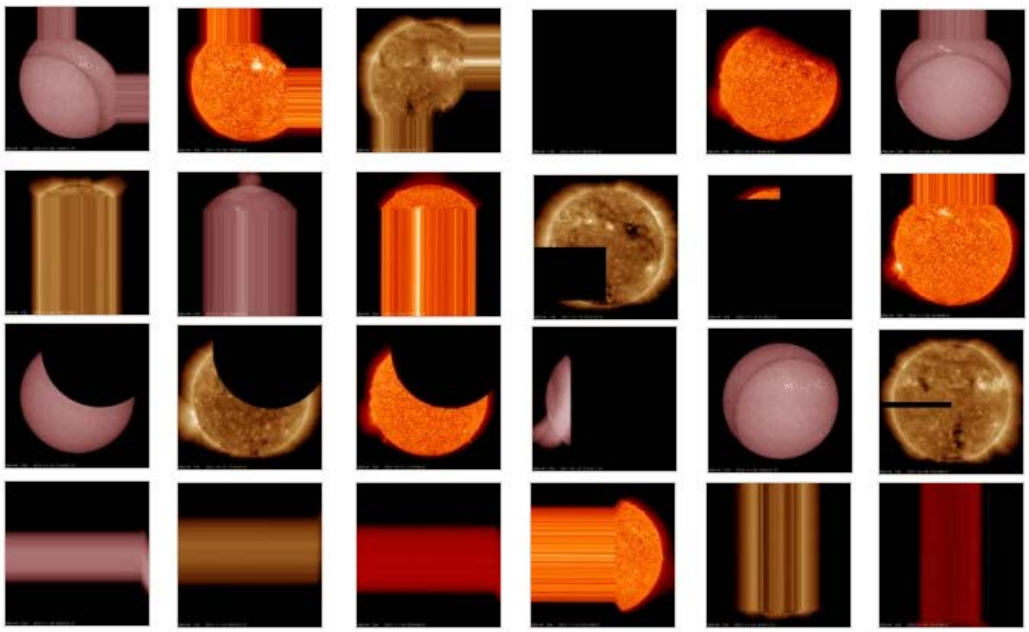

Figure 2: Thumbnails of some of the corrupted AIA images that were downloaded.

3. Detection of active regions and coronal holes from SDO Images

3.1 Fuzzy Theory

Fuzzy theory has been used in wide range of problems and applications since its proposition by Lotfi Zadeh in 1960s. Zadeh {Zadeh, 1965 #287} first introduced the fuzzy set theory to mathematically represent vagueness that naturally exists in imprecise information {Moore, 2001 #288}. For the fuzzy-based modelling of complex systems, the underlying mechanics are presented linguistically rather than mathematically and humans reason not in terms of discrete symbols and numbers but in terms of fuzzy sets, are used. Using fuzzy sets one can define general categories (degree of membership) but not rigid collections.
Fuzzy sets are functions that map a value to a number between zero and one indicating its actual degree of membership. The membership value assigned to an element is not restricted to just two values (crisp set), but can be 0, 1 or any value in-between (fuzzy set). A Mathematical function which defines the degree of an element's membership in a fuzzy set is called *membership function*.

3.2 Constructing Membership Functions

Fuzzy expert systems are modelled based on the experience of real experts. It is important to incorporate such experience in defining the fuzzy membership functions for each input and output.

In this work, the Gaussian distribution function, shown in Equation (1), is used to construct the membership function for the fuzzy detection of active regions and coronal holes:

$$G(x) = \frac{1}{\sigma\sqrt{2\pi}} e^{-\frac{(x-\mu)^2}{2\sigma^2}} \quad (1)$$

Where the mean value is represented byμ, and standard deviation by σ, and where the degree of membership $M(p)$ can be calculated using Equation (2).

$$M(p) = \frac{G(p)}{G(\mu)} = e^{-\frac{(p-\mu)^2}{2\sigma^2}} (2)$$

$M(p)$ of a pixel value p is equal to the ratio of output from Gaussian function $G(x)$ for that pixel value to the mean value that is used to construct the Gaussian distribution.

In order to construct the membership function, regions representing clusters from each image are selected manually using an image processing software and their μ and σ are calculated. The membership function construction is key to fuzzy detection and different selection of cluster boundaries to calculate μ and σ would change membership functions. Other methods such as histogram thresholding {Tobias, 2002 #293}, unsupervised segmentation {Deng, 2001 #292}, or edge detection {Lindeberg, 1998 #294} could also have been used for the initial determination of clusters.

Each region representing clusters are determined using one set of AIA images at the beginning of each month and the average of the calculated μ and σvalues (Table 1) are used for constructing membership functions. During the period of six months, calculated μ and σ values doesn't change too much on AIA images in JPEG format. On the other hand, AIA images in FITS format have larger range of pixel values compared to their corresponding JPEG images, hence their values could fluctuate more over time.

Four different clusters are determined in this study. Membership functions for coronal-hole (CH), active region (AR), quite sun (QS) and Space (S) are constructed separately for each image using the values in Table 1. In JPEG images Greyscale values change between 0-255, hence the values in Table 1 should be re-calculated if FITS images are to be used.

Constructed membership functions are plotted in Figure 3. For each image four membership functions are constructed. As it can be seen from this figure some of the regions of interests are visually separable using their membership functions. On the top plot, membership functions for AIA-1700 images can be seen. In this plot, although CH, AR and QS regions are not very separable, the S region is clearly distinguishable from the rest. As for the middle plot representing membership functions for AIA-0304 images, differences among the membership functions for CH, AR and QS regions exist. However, the S region intersects heavily with CH and QS regions. On the bottom plot CH and QS membership functions are very close to each other while membership functions for AR and S regions are separable. When all the plots are taken into account, it becomes clear that all the membership information when combined can be used to classify our regions of interest.

Table 1: Mean and standard deviation values chosen for constructing membership functions.

Image Type	**AIA -1700**		**AIA-0304**		**AIA-0193**	
Cluster	$\boldsymbol{\mu}$	$\boldsymbol{\sigma}$	$\boldsymbol{\mu}$	$\boldsymbol{\sigma}$	$\boldsymbol{\mu}$	$\boldsymbol{\sigma}$

Coronal Hole	125.3	23.9	30.1	8.45	127.15	16.61
Space	2.83	0.31	44.7	57.3	24.83	44.34
Quite Sun	122.32	24.72	107.51	18.4	146.16	18.81
Active Region	151.1	35.5	214.34	23.3	235.93	17.1

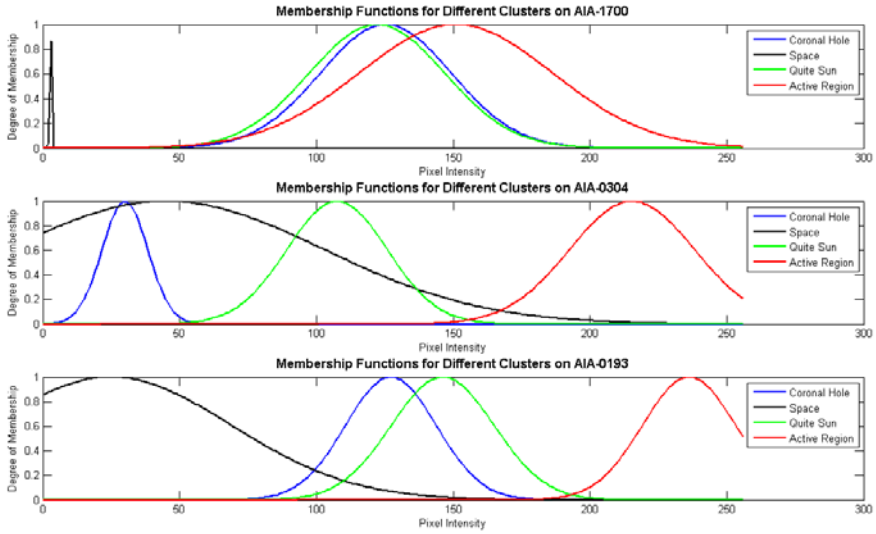

Figure 3: Membership functions for different regions of interest on AIA-1700, 304, and 193 images from top to bottom.

3.3 Feature Detection using Membership Functions

Once the membership functions are defined, Equation (2) is applied to all pixels from all images to determine their degree of membership. As mentioned earlier, the number of membership functions per image is equal to the number of clusters/regions of interest. Hence, each image has four membership functions and each cluster has three degrees of membership (one for each image). For all the corresponding pixels, which have the same location in the three images, the degree of membership values for every cluster are compared and the minimum value is chosen. At the end we will have four values representing the degree of membership of the pixel being processed to four different clusters. These four values are also compared with each other and the pixel is assigned to the cluster with the maximum degree of membership value. Each cluster is given a different label on the output image.

In other words, If $P_I(x,y)$ is the grey scale value of a pixel located at x and y on the input image 'I', where I is one of the three AIA channel images. $P_O(x,y)$ is the label of the clusters at location x and y on the output image 'O', $M_{IC}(P)$ is the membership function value for each cluster 'C' in image 'I':

When

$$MIN(C) = \text{Minimum}\left(M_{IC}(P_I(x,y))\right),\ I \in \{AIA\ 1700, 304, 193\} \quad (3)$$

And

$$\text{MAX=Maximum (MIN(C)), C } \in \{\text{CH, S, QS, AR}\} \quad (4)$$

Then

$$P_O(x,y) = \begin{cases} \text{AR}, & \text{MAX} = \text{MIN(AR)} \\ \text{S}, & \text{MAX} = \text{MIN(S)} \\ \text{QS}, & \text{MAX} = \text{MIN(QS)} \\ \text{CH}, & \text{MAX} = \text{MIN(CH)} \end{cases} \quad (5)$$

Using Equations 3, 4, and 5, the pixel values for the output image can be determined. In this study red, black, grey and blue coloured labels are assigned for AR, S, QS, and CH clusters, respectively.

4. Results and Comparison with EVE Data

The feature detection algorithm described earlier is applied to 8800 sets (each set is composed of three different channels) of images from1stOctober 2010 to 31st March 2011. This data set is formed after eliminating the corrupted images which were around 10% of the overall images (around 45,000) and using channels only when the time difference is less than one minute. In Figure 4the output from the algorithm for the image set shown in Figure 1 is provided. In this figure grey areas represent QS, blue areas represent CH, red areas represent AR, and black areas represent S. ARs are discretely visible both on AIA 304 and 193 images and it is expected that the detected AR clusters are a combination of areas on both channels. For CH almost all the information is coming from AIA 193 and the output is visually very similar to the previously selected coronal hole areas in order to determine the fuzzy variables.

The filling factors (FF) or ratio of clusters' area to the total solar disk area is also calculated for the output of each image set. Using this output, the plot in Figure 5 is constructed using linear interpolation for the missing data points. A FF value for AR and CH every 0.01 Julian day is calculated using linear interpolation which is every 14.4 minutes. One minute data from EVE/ESP is also plotted on Figure 6. If we compare these two plots visually it is clear that peaks and valleys in FF values for the AR cluster is very similar to ESP 171 and 257 irradiance measurements which is not the case for FF values for CH cluster.

This relation between AR and irradiance measurements can be demonstratedbetter in Figure 7 where one minute irradiance measurements are also interpolated to provide samples every 0.01 Julian day. When we zoom in to show the FFs of ARs and irradiance measurements between 16thand 21st October (where minimal missing or corrupted data exist), the similarity between the two signals becomes clearer, even for small changes in both signals. This encouraged us to investigate whether irradiance measurements could be predicted from the FF of ARs.

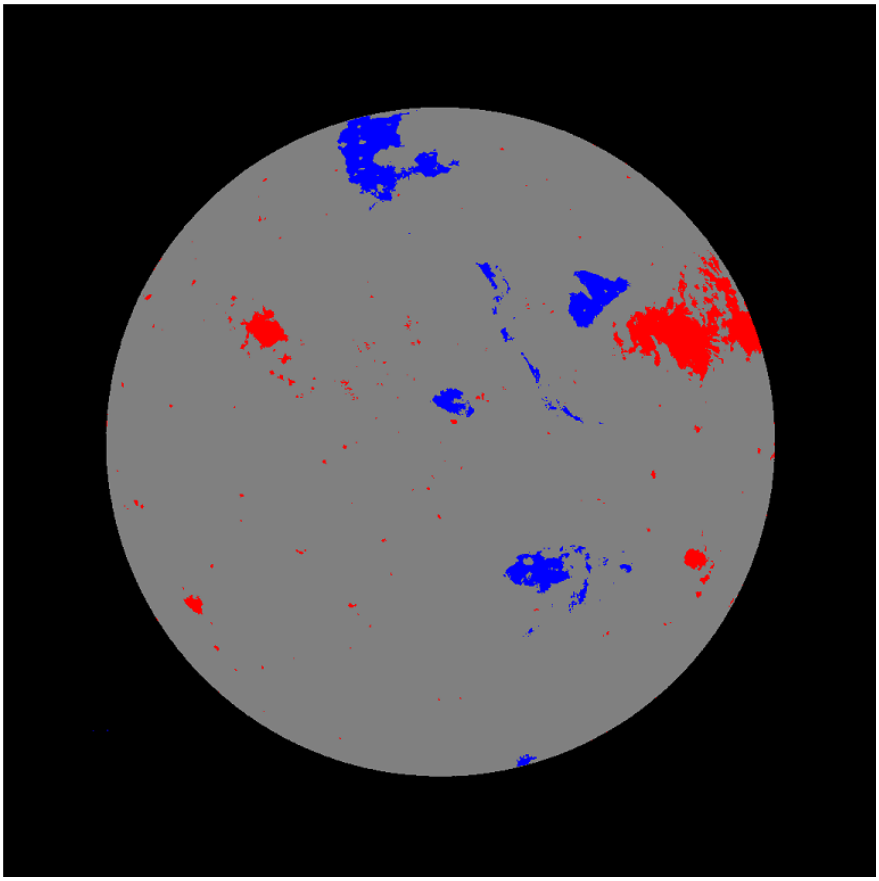

Figure 4: Result of segmentation using fuzzy method.

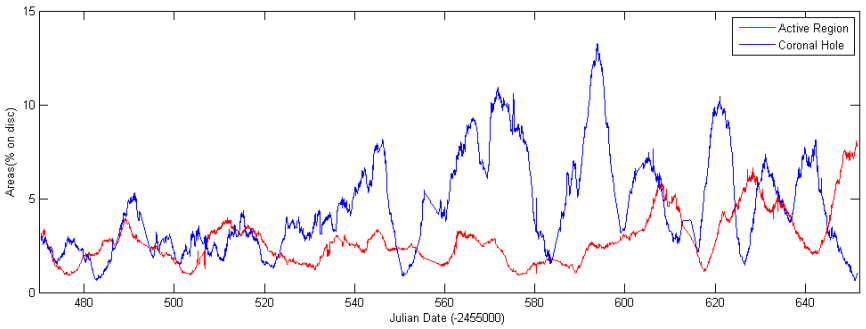

Figure 5: Ratio of areas for detected solar feature clusters to solar disk.

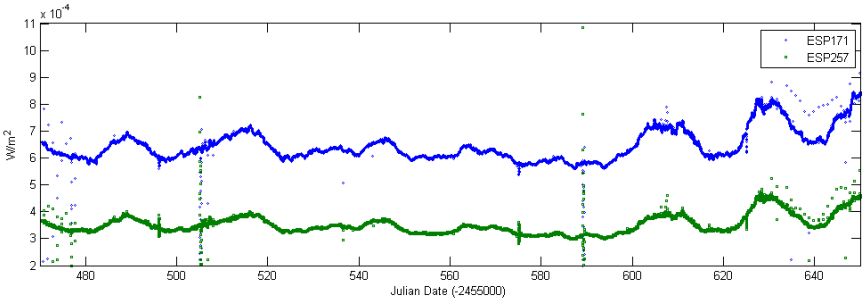

Figure 6: Two channels (near 17.1nm and 25.7 nm) of EVE/ESP irradiance measurements.

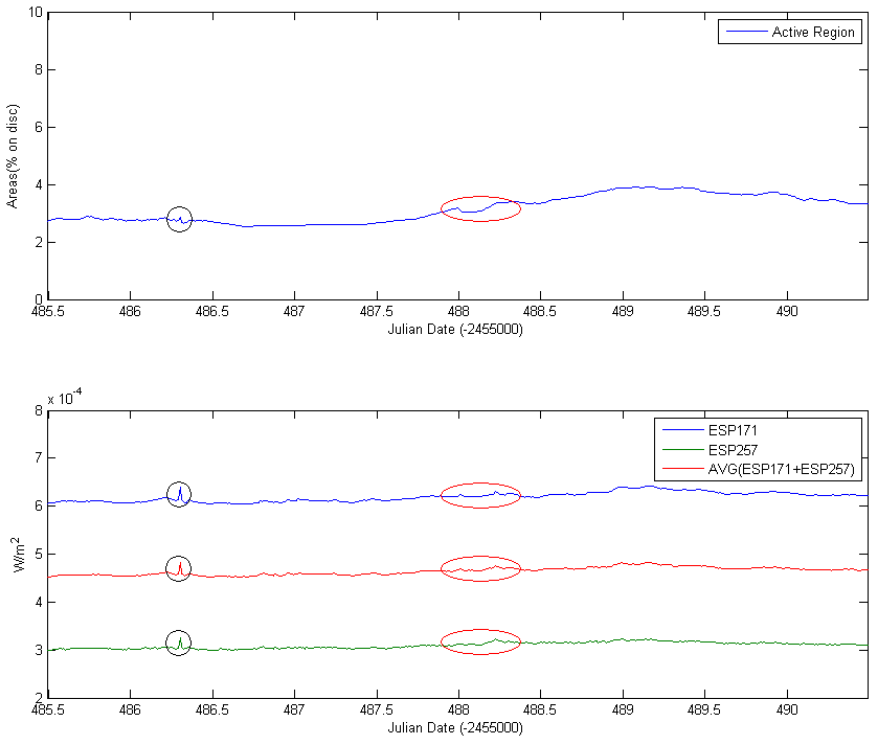

Figure 7: Zoomed in comparison of active region ratios to two channels of EVE/ESP irradiance measurements. Similarities are marked.

5. Prediction/Construction of Irradiance

In order to see if irradiance measurements can be predicted or constructed using the extracted FF data from solar images Radial Basis Function Networks (RBFNs) are used. In the following sub section this process and its results are presented.

5.1 Radial Basis Function Networks (RBFNs)

RBFNs are powerful interpolation techniques that can be efficiently applied in multidimensional- space problems. The RBFN approach to classification is based on curve fitting. Learning is achieved when a multi-dimensional surface is found that can provide optimum separation of the multi-dimensional training data. In general, RBFNs can model continuous functions with reasonable accuracy {Qahwaji, 2007 #215}.
The output of an RBFN is represented as:

$$f(x) = \sum_{j=1}^{N} \propto_j \emptyset(\|x - x_j\|) \qquad (6)$$

Where x is an input vector and α_j represents the weights associated with each training data point x_j.$\phi(\cdot)$ is a radial basis or kernel function centred at x_j, which defines the influence of each training data point on the output value. The radial basis functions are the set of functions provided by the hidden nodes that constitute an arbitrary "basis" for the input patterns {Qu, 2003 #38}. Details on the theory and the implementation of RBFN can be found in {Qu, 2003 #38} and {Sutton, 1998 #196}.

5.2 Training and Prediction Data Sets

The prediction capability of the RBFN system for EVE/ESP irradiance measurements in two channels (17.1 and 25.7 nm) is tested using the six months FF data that was created using our fuzzy system.

The RBFN toolkit in MATLAB is used for training and prediction/evaluation. From the six months of data, the first 20 days of October 2010 and the last 20 days of March 2011are separated and used for training the RBFN system, while the rest of the data are used for the prediction and evaluation of the prediction results. The level of solar activity was higher towards the end of the six months period and in order to train the RBFN system with different kind of data and achieve better predictions, the training data is created by combining extracted FF data from different months (first and the last 20 days of the six month period).

Two training and prediction/evaluation data sets with different time intervals (0.01 and 0.1 Julian day) are created for each channel (17.1, 25.7 nm) of irradiance measurements. The models in Figure 8 are used for time series prediction. The training data is created by using the FF data extracted from the three AIA channels and their corresponding EVE/ESP irradiance measurements (Figure 5 and 6).

For 0.01 Julian day intervals, the RBFN model shown on the left hand side of Figure 8 is used. This model uses four consecutive AR FF data as input and one ESP data representing output. The first training pair in the data set is formed by including four consecutive AR FF data from Julian date 2455470.50 to 2455470.54 as inputs and ESP data from Julian date 2455470.55as output. The second training pair is formed by including four consecutive AR FF data starting from Julian date 2455470.51 to 2455470.55 as inputs and ESP data from Julian date 2455470.56 as output. The rest of the training pairs are formed in the same way by extracting corresponding data every 0.01 Julian days for the first and the last 20 days of the six month period.

For 0.1 Julian day intervals, the RBFN model shown on the right hand side of Figure 8 is used. The first training pair in the data set is formed by including two consecutive AR FF data from Julian date 2455470.5 to 2455470.6 as inputs and ESP data from Julian date 2455470.7as output. The second training pair is formed by including two consecutive AR FF data starting from Julian date 2455470.6 to 2455470.7 as inputs and ESP data from Julian date 2455470.8 as output. This process is repeated for the rest of the training pairs by extracting relevant data every 0.1 Julian days for the first and the last 20 days of the six month period.

The remaining data that is not used for training are used for evaluating the prediction capability of the RBFN system. The prediction data are created in the manner described above (without the ESP data) and is fed to the trained RBFN system. The generated predictions are compared with the real outputs.

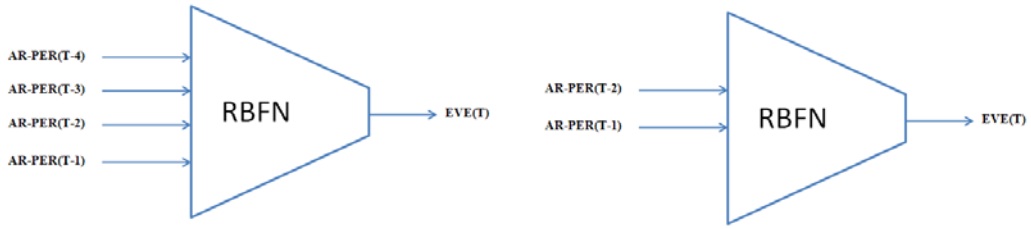

Figure 8: RBFN model used for time series prediction of irradiance measurements from EVE/ESP. AR-PER represent Active Region percentage on disc. T represents given time. Left: Model used for 0.01 Julian day time intervals. Right: Model used for 0.1 Julian day time intervals.

5.3 Prediction Results

Plots comparing the predicted and real ESP irradiance measurements near 17.1 and25.7 nm in 0.01 and 0.1 Julian day intervals are given in Figures 9 and10, respectively. In this figures, top plots show comparisons of predicted irradiance measurements with real measurements in 0.01 Julian day intervals while bottom plots show the predicted and real measurements for 0.1 Julian day intervals. Average error rates for the predicted irradiance measurements in different time intervals are provided in Table 2.These error rates are calculated by dividing the difference between the predicted and the real data values by the real data values.

It should be emphasised that although the difference between the predicted and the real values appears to be large (due to the scaling used on y(irradiance)-axis) the average error rates in fact never exceeds 5% for all the data sets.The average error rate is approximately one percent lower for ESP 171predictions compared with ESP 257 predictions. However, the average error rates for both ESP 171 and 257 are still acceptable. Its worth noting that the RBFN uses smaller training sets compared to the prediction/evaluation setsdue to data point restrictions in Matlab RBFN toolkit (Maximum 5000 data points can be used for training).

Training these RBFN models with more data would provide better prediction results but the average error rates still shows that AR filling factors can be used for the prediction of ESP irradiance measurements or the construction of missing irradiance measurements, especially for similar wavelengths.

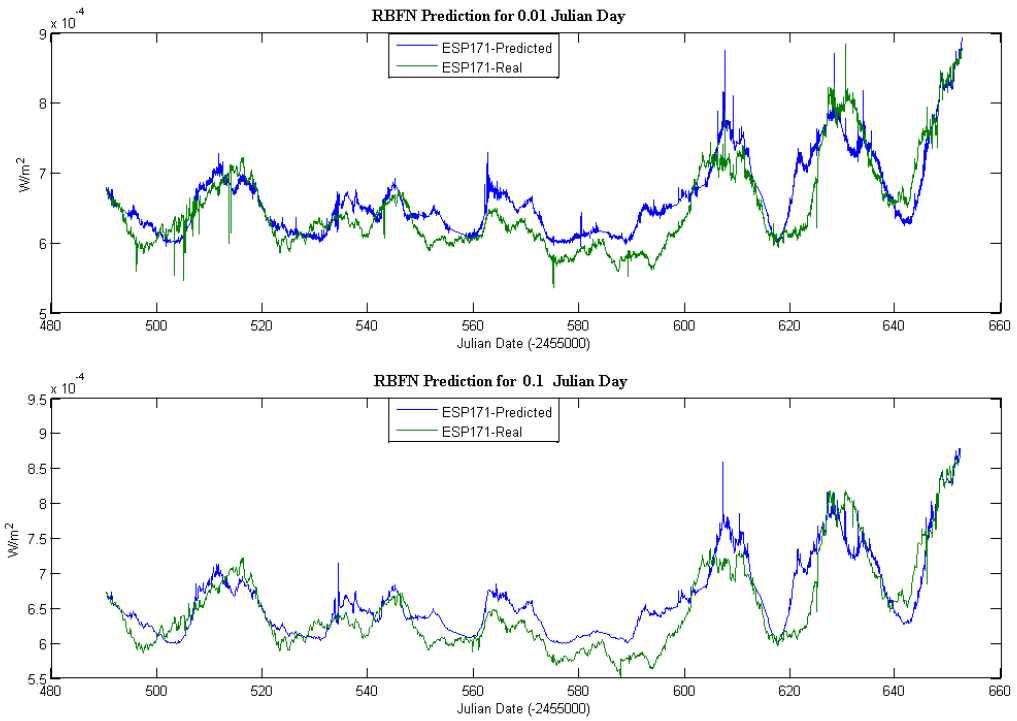

Figure 8: Comparison of predicted EVE/ESP 171 irradiance measurement near 17.1 nm to real ones. Top: Data sampled for 0.01 Julian days. Bottom: Data sampled for 0.1 Julian days.

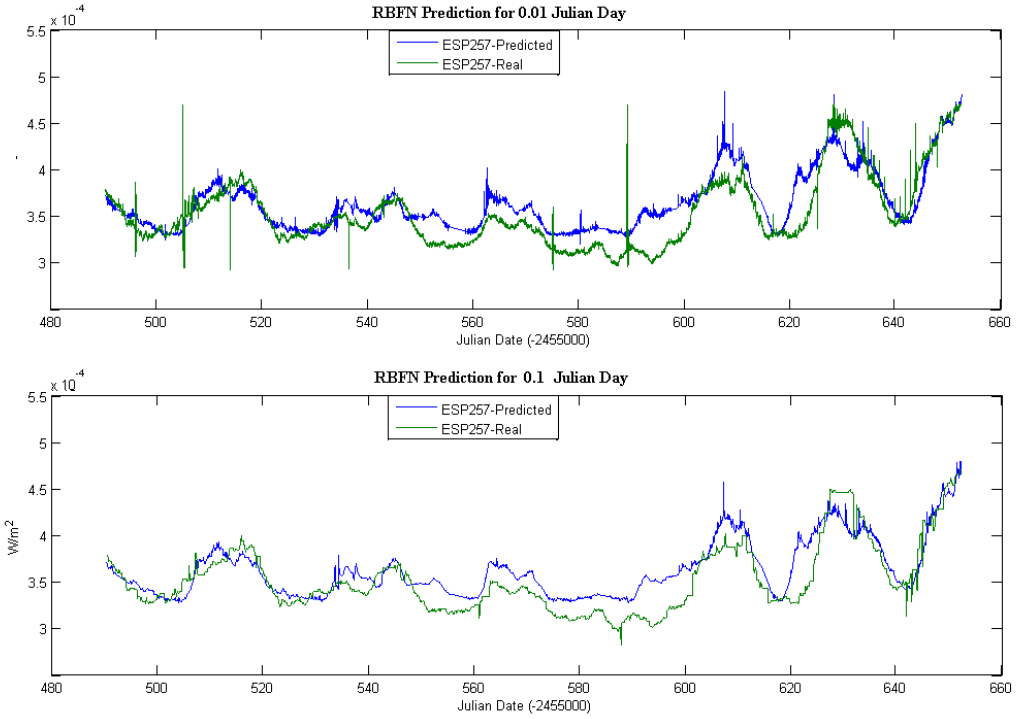

Figure 9: Comparison of predicted EVE/ESP 257 irradiance measurement near 25.7 nm to real ones. Top: Data sampled for 0.01 Julian days. Bottom: Data sampled for 0.1 Julian days.

Table 2: Average error rates for the predicted irradiance measurements in different time intervals. CP: Channel Predicted. TI: Time Interval in Julian day. TNDP: Total Number of Data Points. NDPUT: Number of Data Points Used for Training. NDPUP: Number of Data Points Used for Prediction. AE: Average Error Rate.

CP	TI	TNDP	NDPUT	NDPUP	AER
171	0.01	18200	4000	14200	3.97%
	0.1	1820	400	1420	3.93%
257	0.01	18200	4000	14200	4.91%
	0.1	1820	400	1420	4.78%

6. Conclusions and Discussions

In this study a simple fuzzy algorithm for the automatic detection of selected solar features from multi channel SDO/AIA images is provided. This algorithm can be easily adapted for the automated and simultaneous processing of different SDO/AIA channels to create any amount of clusters within an image. AIA-193, AIA-304, and AIA-1700 channels from1stOctober 2010 to 31st March 2011 are processed at the same time to create an output image with CH, AR, SD, and S clusters. Then CH and AR clusters are used to calculate the ratio of their areas compared to the total solar disk area (CH+AR+QS) which is generally known as filling factors (FF).

AR FF shows high correlation with EVE/ESP irradiance measurements near 17.1 and 25.7 nm in micro level which encouraged us to design a time series prediction system using RBFN. Four RBFN systems; for the prediction of 17.1 and 25.7 nm irradiance measurement in two different time intervals are modelled and trained using AR FF data from the first and the last 20 days of the six months period and their corresponding EVE/ESP irradiance measurements.

Both EVE/ESP irradiance measurements are predicted in 0.01 and 0.1 Julian day intervals; while the former uses the last four filling factors calculated for AR to predict ESP irradiance measurements, the later uses the last two filling factors.

Prediction results for ESP measurements for 17.1 and 25.7 nm wavelengths looks very promising with an average error less than 5%. When we take into account that the AR clustering decision is mainly made by combining the membership functions for AIA images in 19.3 and 30.4 nm, this shows that AR data extracted from AIA images can be used to construct or predict missing data from irradiance measurements, especially from images closer to the measurements wavelength, with higher accuracy. The relation between the AR filling factors and other indices for irradiance measurements such as the F10.7, Magnesium II index from other satellites needs to be investigated further. AIA and EVE instruments are both on SDO and this might help improve the accuracy of predictions.

AR clusters can be detected separately from each AIA channel using the method described here (e.g. by just using AIA 1700 with 304, or AIA 1700 and 193) and AR filling factors can be calculated for each wavelength separately. This can be useful to investigate the relation between the data available in images and irradiance measurements with different wavelengths.

Although 1K × 1K images are used in this work higher resolution images can be processed using the method described here without the need for

changes/modifications. Computational time increases linearly with the number of pixels in an image (Figure 11) and the number of channels processed simultaneously. The fuzzy method described here is also suitable for parallel computing where every set of pixels can be processed on a separate processing unit and combined together at the end without using complex algorithms. For example, the processing time for 4K × 4K images is around 16 seconds using the method described in this paper and dividing images to four and processing on four different processors will reduce this time to around four seconds.

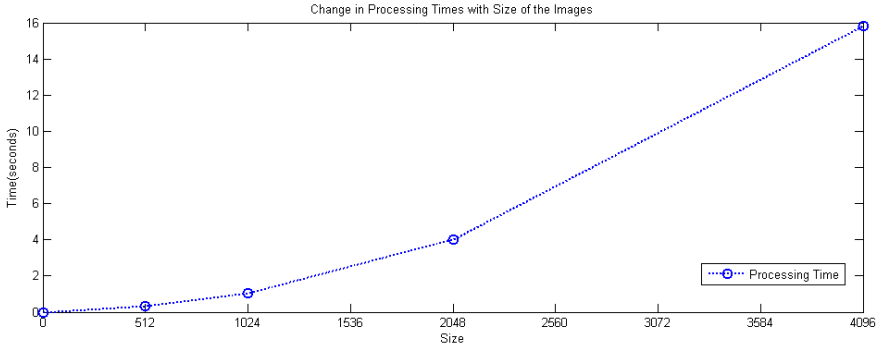

Figure 10: Computational performance of the method for different size of images.

Solar radiation from radio waves and visible light to the ultraviolet, X-rays, and gamma-rays, affects space weather in short terms and global climate in longer terms. Variations of the solar irradiance are the fundamental forcing mechanisms to the terrestrial atmosphere, land, and oceans {Tobiskaa, 2000 #295}. It is important to understand the variations in the solar irradiance and its impact on space weather. Currently EVE is providing high cadence measurements of the EUV irradiance and data from EVE can be used to understand how and why the solar EUV spectral irradiance varies. This is a key for the long or short term forecasting of space weather events. To be able to predict solar irradiance partly or fully from solar images with high accuracy could help us to construct solar irradiance measurements that were missing in the past or will be missing in the future because of instrument failures. Also the predicted irradiance measurements could be used to drive other space weather models.

Acknowledgement

This work is supported by an EPSRC Grant (EP/F022948/1), which is entitled 'Image Processing, Machine Learning and Geometric Modelling for the 3D Representation of Solar Features'.

References